Acta Pharmaceutica Sinica B 2022;12(9):3513−3528

Chinese Pharmaceutical Association
Institute of Materia Medica, Chinese Academy of Medical Sciences

Acta Pharmaceutica Sinica B

www.elsevier.com/locate/apsb
www.sciencedirect.com

ORIGINAL ARTICLE

Critical involvement of lysyl oxidase in seizure-induced neuronal damage through ERK-Alox5-dependent ferroptosis and its therapeutic implications

Xiaoyuan Mao[a,b,c,d,*], Xuan Wang[e], Mingzhu Jin[f], Qin Li[a,b,c,d], Jining Jia[a,b,c,d], Menghuan Li[e,h], Honghao Zhou[a,b,c,d], Zhaoqian Liu[a,b,c,d,*], Weilin Jin[g,*], Yanli Zhao[h,*], Zhong Luo[e,*]

[a]*Department of Clinical Pharmacology, Xiangya Hospital, Central South University, Changsha 410008, China*
[b]*Institute of Clinical Pharmacology, Central South University, Hunan Key Laboratory of Pharmacogenetics, Changsha 410078, China*
[c]*Engineering Research Center of Applied Technology of Pharmacogenomics, Ministry of Education, Changsha 410078, China*
[d]*National Clinical Research Center for Geriatric Disorders, Changsha 410008, China*
[e]*School of Life Science, Chongqing University, Chongqing 400044, China*
[f]*Department of Gynecology and Obstetrics, Xin Hua Hospital Affiliated to Shanghai Jiao Tong University School of Medicine, Shanghai 200092, China*
[g]*Institute of Cancer Neuroscience, Medical Frontier Innovation Research Center, the First Hospital of Lanzhou University, the First Clinical Medical College of Lanzhou University, Lanzhou 730000, China*
[h]*Division of Chemistry and Biological Chemistry, School of Physical and Mathematical Sciences, Nanyang Technological University, Singapore 637371, Singapore*

Received 20 January 2022; received in revised form 18 April 2022; accepted 24 April 2022

KEY WORDS

Drug delivery;
Ferroptosis;
Lysyl oxidase;

Abstract Recent insights collectively suggest the important roles of lysyl oxidase (LysOX) in the pathological processes of several acute and chronic neurological diseases, but the molecular regulatory mechanisms remain elusive. Herein, we explore the regulatory role of LysOX in the seizure-induced ferroptotic cell death of neurons. Mechanistically, LysOX promotes ferroptosis-associated lipid peroxidation in neurons *via* activating extracellular regulated protein kinase (ERK)-dependent 5-lipoxygenase (Alox5)

*Corresponding authors.
E-mail addresses: xiaoyuanm@csu.edu.cn (Xiaoyuan Mao), zqliu@csu.edu.cn (Zhaoqian Liu), ldyy_jinwl@lzu.edu.cn (Weilin Jin), zhaoyanli@ntu.edu.sg (Yanli Zhao), luozhong918@cqu.edu.cn (Zhong Luo).
Peer review under responsibility of Chinese Pharmaceutical Association and Institute of Materia Medica, Chinese Academy of Medical Sciences.

https://doi.org/10.1016/j.apsb.2022.04.017
2211-3835 © 2022 Chinese Pharmaceutical Association and Institute of Materia Medica, Chinese Academy of Medical Sciences. Production and hosting by Elsevier B.V. This is an open access article under the CC BY-NC-ND license (http://creativecommons.org/licenses/by-nc-nd/4.0/).

Neuronal damage;
Seizure

signaling. In addition, overexpression of LysOX *via* adeno-associated viral vector (AAV)-based gene transfer enhances ferroptosis sensitivity and aggravates seizure-induced hippocampal damage. Our studies show that pharmacological inhibition of LysOX with β-aminopropionitrile (BAPN) significantly blocks seizure-induced ferroptosis and thereby alleviates neuronal damage, while the BAPN-associated cardiotoxicity and neurotoxicity could further be reduced through encapsulation with bioresponsive amorphous calcium carbonate-based nanocarriers. These findings unveil a previously unrecognized LysOX-ERK-Alox5 pathway for ferroptosis regulation during seizure-induced neuronal damage. Suppressing this pathway may yield therapeutic implications for restoring seizure-induced neuronal injury.

© 2022 Chinese Pharmaceutical Association and Institute of Materia Medica, Chinese Academy of Medical Sciences. Production and hosting by Elsevier B.V. This is an open access article under the CC BY-NC-ND license (http://creativecommons.org/licenses/by-nc-nd/4.0/).

1. Introduction

Seizures are caused by abnormal and synchronous neuronal activity of a population of neuronal cells, leading to well-characterized behavioral manifestations such as tonic-clonic movement, convulsions and cognitive impairment. Seizure is clinically associated with a wide range of acute and chronic neurological conditions including epilepsy, brain tumor, ischemic stroke, autism and neurodegenerative diseases[1−6]. Neuronal injury is a characteristic neuropathologic change after seizures in human epilepsies[7], which often induces functional and structural changes in the neuronal network[8]. Accumulating evidence strongly supports that repetitive seizure can activate neuronal death process, contributing to neuronal damage. Seizure-induced hippocampal damage has been reported to increase the episode of recurrent seizures and the frequency of severe epileptic seizures[9]. Elucidating the post-seizure neuronal death mechanism would yield novel therapeutic approaches for seizure treatment.

Studies suggest that ferroptosis, a novel form of iron-dependent regulated cell death characterized by abnormal accumulation of lethal lipid peroxides, has been implicated in many disease conditions including cancers, ischemic or metabolic diseases and neurodegenerative disorders[10−15]. Ferroptosis presents a series of distinct morphological, genetic and biochemical traits compared with other cell death modes like apoptosis, autophagy and necroptosis[15]. We previously provided direct evidence showing ferroptotic events in various seizure models induced by kainic acid (KA), pentylenetetrazole (PTZ), pilocarpine (Pilo) and $FeCl_3$[16−19]. Pharmacological inhibition of ferroptosis with ferrostatin-1 (Fer-1) or liproxstatin-1 (Lip-1) remarkably suppressed seizure activity, suggesting a promising approach in seizure control *via* targeting ferroptosis. However, the detailed regulatory mechanism of ferroptosis after seizure induction remains unknown.

Lysyl oxidase (LysOX) is an endogenous enzyme responsible for the crosslinking of extracellular matrix (ECM) to maintain its tensile strength and structural integrity[20,21]. Interestingly, latest insights demonstrate that LysOX is also involved in the aspects of epithelial-to-mesenchymal transition (EMT), gene transcription and embryogenesis[22−24]. There are also other reports that LysOX may affect certain neurologic diseases such as Alzheimer's disease, hereditary cerebral hemorrhage as well as amyotrophic lateral sclerosis[25−27]. However, the function of LysOX in seizure-induced neuronal injury remains to be investigated.

Herein, we report that LysOX levels in neurons in kainic acid (KA)-induced seizure mice were significantly elevated while neuron-specific LysOX deletion inhibited ferroptosis therein. Mechanistically, LysOX stimulates ferroptosis *via* activating extracellular regulated protein kinase (ERK) to trigger 5-lipoxygenase (Alox5) phosphorylation, subsequently leading to lipid ROS accumulation, whereas inhibiting LysOX with β-aminopropionitrile (BAPN) ameliorated neuronal damage in a KA-treated mouse seizure model. Furthermore, to assess the clinical translation potential of BAPN-based therapy, we systematically evaluated the safety of BAPN and found that it has evident toxic effects, especially against the heart and nerve system. To minimize the side effects of BAPN, we adopted the brain targeting drug delivery nanotechnology, which is a promising therapeutic approach against neurological diseases such as epilepsy[28], glioma[29] and brain metastasis[30]. Our results illustrated that BAPN-associated cardiotoxicity and neurotoxicity were efficiently abrogated through encapsulation with bioresponsive amorphous calcium carbonate-based nanocarriers. Altogether, our results show that elucidation of the post-seizure neuronal ferroptosis mechanisms offers new paradigms for alleviating brain damage in diverse neurological conditions such as epilepsy. We also highlight LysOX/ERK/Alox5 signaling axis as the mechanistic base of neuronal ferroptosis after seizures. Suppression of LysOX-mediated ferroptosis process may provide a novel therapeutic approach for combating neuronal injury caused by seizure disorders such as epilepsy.

2. Materials and methods

All the chemicals and virus strains were summarized in Supporting Information Fig. S1. The product quality, if available, was also displayed in Fig. S1.

2.1. Mice

Male adult mice were selected in our present work, except that the results should be obtained in different groups from either male or female mice at five time points including 4, 5, 6, 7 and 8 weeks of age. C57 BL/6J and BALB/c mice were obtained from the Animal Center of Central South University (Changsha, China). *LysOX*-floxed (*LysOX*$^{fl/fl}$) mice were supplied by Biocytogen Technology (Beijing, China). *Map2*-Cre mice with C57 BL/6J background expressing neuron-specific Cre topoisomerase were provided by Shanghai Model Organism (Shanghai, China). Mice were housed in individual cages under an atmospheric temperature of 24 ± 2 °C and a day/night cycle of 12 h. All animal handling protocols have been reviewed and approved by the Animal Care and Use Committee of Central South University under the license of 2019-0004 (Changsha, China). We ensure

that all protocols strictly followed the ethics guidelines established by the National Institute of Health for the Care and Use of Laboratory Animals.

Tamoxifen-inducible *LysOX* knockout (designed as *LysOX* KO) mice were obtained by breeding *LysOX*-floxed mice with *Map2*-Cre ones. *LysOX* KO mice were back-crossed into with the purpose of obtaining a constant C57BL/6J background. To obtain neuron-specific *LysOX* KO mice, animals were intraperitoneally injected with tamoxifen (dissolved in corn oil at the concentration of 2.5 mg/mL) once a day for five successive days at a daily dose of 75 mg/kg.

2.2. Cell culture

HT22 cell, an immortalized hippocampal cell line, was incubated in Dulbecco's modified Eagle's medium with high glucose supplemented with 10% fetal bovine serum (FBS), penicillin (100 U/mL) and streptomycin (100 μg/mL). The cells were placed in an incubator with 5% CO_2 atmosphere at 37 °C.

2.3. Establishing KA-treated seizure mouse model

The protocol of KA-triggered seizure mouse model was adapted from a previous study[18]. For short, male C57BL/6J mice (6−8 weeks of age) were anesthetized with sodium phenobarbital (50 mg/kg, i.p.) and immobilized on a stereotaxic apparatus. Using a syringe pump and an infusion needle (62204, RWD Life Science, Shenzhen, China), KA (1 μL, 250 ng/μL dissolved in saline) was stereotactically injected into the right hippocampus (coordinates anteroposterior −2.0 mm; lateral −1.3 mm; dorsoventral −1.2 mm). The needle would remain at the injection site for another 5 min after completing the KA injection to prevent reflux. In control group, saline (1 μL) was infused. At the early stage after KA injection, animals exhibited discrete seizures, followed by prolonged seizures[31]. Status epilepticus (SE) onset was defined as prolonged seizures with spike frequency greater than 3 Hz[32]. Behavioral and electrographic seizures were monitored after the last drug or vehicle injection. Thirty minutes after SE induction, mice were individually treated with: BAPN (dissolved in saline with the dose of 50 or 100 mg/kg, intraperitoneal injection for seven days), Lip-1 (dissolved in 1% dimethyl sulfoxide with the dose of 10 mg/kg, and intraperitoneal injection for three times at three different time points), U0126 (dissolved in 1% dimethyl sulfoxide with the dose of 30 mg/kg, intraperitoneal injection 1 h prior to KA) and Zileuton (dissolved in 1% dimethyl sulfoxide with the dose of 35 mg/kg, intraperitoneal injection 1 h prior to KA). The dosage and dosing frequency were selected according to previous descriptions[33−38]. Mice that showed stage 4 or 5 seizures by Racine score system[39] were recruited into our study.

2.4. Nissl staining

Brain tissue sections (10 μm) from each group were stained with Nissl staining solution (C0117, Beyotime Biotechnology, China) for 10 min. After dehydration, brain sections were imaged using an optical microscope (Leica, Germany).

2.5. Fluoro-Jade B (FJB) assay

Tissue slides (10 μm) were soaked with 1% sodium hydroxide and 70% ethanol for 5 min and 2 min, respectively. Subsequently, the samples were incubated with 0.06% potassium permanganate for about 10 min. Following several thorough washes, 0.0004% FJB solution (AAT Bioquest, USA) was employed to immerse the slides for 20 min. Afterward, tissue sections were coverslipped with neutral balsam and viewed under a fluorescence microscope. Degenerated neurons were calculated using Image J software (Bethesda, MD, USA).

2.6. Transmission electron microscopy (TEM)

Mice were treated with phosphate-buffered saline (PBS) at pH 7.4 *via* cardiac perfusion and then sacrificed to extract the brains, which were carefully dissected and cut into thin sections with an average thickness of 100 nm. The brain tissue sections were stained by uranyl acetate and lead citrate. Samples were then imaged on a TEM (JEM2000EX, Tokyo, Japan).

2.7. Determination of GSH content

GSH level was determined with a commercial kit (S0053, Beyotime Biotechnology, China) *via* procedures described in the manual.

2.8. Determination of mRNA expression by real-time PCR

Total RNA from tissues or cells was obtained *via* the TRIzol method. Following the reverse transcription into cDNA, all samples were assayed by real-time PCR. Gene expressions were calculated using $2^{-\Delta\Delta CT}$ method. The associated primer sequences were displayed in Supporting Information Fig. S2.

2.9. Western blot assay

Tissue or cell protein extracts were obtained using a cold lysis buffer (P0013, Beyotime Biotechnology Institute, China) with mixed protease and phosphatase inhibitors. Equal amount of protein (20 μg) from different groups was separated by gel electrophoresis and membrane transferring. Then, the membranes were blocked with 5% non-fat milk for 1 h and subsequently rinsed with primary antibodies including 4-hydroxynonenal, LysOX, cleaved caspase-3, LC3II/I, glutathione peroxidase 4 (GPX4), phosphor-ERK, total ERK, phosphor-JNK, total JNK, phosphor-p38, total p38, Alox5 (Ser663) and total Alox5, while β-actin or α-tubulin were used as control. Other details of antibodies were summarized in Supporting Information Fig. S3.

2.10. Malonaldehyde (MDA) analysis

MDA level was analyzed by a commercially available assay kit (S0131, Beyotime Technology Institute, China) *via* procedures described in the user manual.

2.11. Measurement of lipid peroxide levels

Lipid peroxidase (LPO) of tissues and cells was assayed by a kit from Jiancheng Biotechnology (A106, China) by monitoring the absorbance at 586 nm. Cellular lipid peroxide levels were carried out according to a previously reported method[38]. HT22 cells after different treatment were trypsinized and incubated with BODIPY™ 581/591 C11 (2 μmol/L) for 15 min. Fluorescence signal was analyzed under a flow cytometer under 488 nm excitation wavelength.

2.12. Propidium iodide (PI)/Hoechst33342

After 12 h of cultivation, HT22 cells were incubated with 1 mmol/L BAPN (LysOX inhibitor, 30 min after glutamate or erastin), 10 μmol/L U0126 (ERK inhibitor, pretreatment 1 h prior to glutamate or erastin), 10 μmol/L Zileuton (Alox5 inhibitor, co-treatment with glutamate or erastin), 10 μmol/L SP600125 (JNK inhibitor, pretreatment 1 h prior to glutamate or erastin) or 10 μmol/L of SB203580 (p38 inhibitor, pretreatment 1 h prior to glutamate or erastin). Cells incubated with 5 mmol/L glutamate or 500 nmol/L erastin was used as model group. Thereafter, cells were co-stained with Hoechst 33342 (5 μg/mL) and PI (5 μg/mL) for 5 min. Images were captured using a fluorescence microscope (Leica, Germany).

2.13. Cell death assessment

To assess the treatment-induced cell death, HT22 cells from each group were stained with PI for 15 min and the fluorescence signal was obtained at the excitation wavelength of 488 nm on a flow cytometer (Beckman, USA).

2.14. Determination of cell viability by cell counting kit 8 (CCK8)

HT22 cells were first treated with Lip-1, Fer-1, deferoxamine (DFO), 3-methyladenine (3-MA), necrostatin-1 (Nec-1) or benzyloxycarbonyl-Val-Ala-Asp (OMe) fluoromethylketone (Z-VAD-FMK) for 2 h, and then with glutamate for additional 8 h. Thereafter, cells were incubated with CCK8 reagent (10 μL, C0038, Beyotime Biotechnology Institute, China) solubilized in a culture medium (100 μL) at 37 °C for 2 h. The absorbance was analyzed at 450 nm.

2.15. Detection of LysOX activity

LysOX activity was detected by an assay kit (ab112139, Abcam, UK) based on the standard protocol.

2.16. Gene knockdown

The knockdown of selected genes was performed by RNA interference technique. Small interfering RNAs (siRNA) were provided by RioBio Biotechnology (Guangzhou, China) and the target sequences were listed in Fig. S2. When the confluence reached around 40%, HT22 cells were transfected *via* adding mixed reagents including Lipofectamine™ RNAiMAX and siRNA. Following transfection for two days, cells were digested and cultivated in 24- or 96-well plates, which were subjected to glutamate or erastin challenge.

2.17. Confocal microscopy

Following transcardial perfusion with PBS, brain samples were extracted and carefully dissected, which were further cut into tissue slides with an average thickness of 8 μm using a cryostat (CM1900UV, Leica, Germany) followed by incubation with 0.2% Triton X-100 and 5% donkey serum in PBS. Then, the primary antibody was added to incubate the sections overnight. On the next day, the slices were washed and treated with the secondary antibody for 1 h. Fluorescent images were captured under a confocal laser scanning microscope (Nikon, Japan). The detailed information of antibodies was indicated in Fig. S3.

2.18. In vivo LysOX overexpression

Overexpression of *LysOX* in the hippocampus was achieved *via* AAV method. The plasmid-integrated AAV-PHP.eB vectors were obtained from Obio Technology (Shanghai, China). For the implementation of AAV-mediated gene transfer, a microsyringe pump (R452, RWD Life Science, Shenzhen, China) was employed for the stereotaxical injection of AAV-SYN-LysOX-P2A-EGFP-3FLAG (0.5 μL, virus titers: 1.04×10^{12} vg/mL) or AAV-SYN-EGFP-3FLAG (0.5 μL, virus titers: 0.75×10^{12} vg/mL) into the right hippocampus (mediolateral −1.3 mm; anteroposterior −2.00 mm; dorsoventral: −1.2 mm) at a flow rate of 4.6 nL/6 s. Four weeks after AAV injection, three animals per group were sacrificed to monitor the LysOX expression levels *via* immunofluorescence.

2.19. Preparation and characterization of $CaCO_3$@BAPN-CaSi-PEG-TAT

The preparation of $CaCO_3$@BAPN-CaSi-PEG-TAT includes five steps. Firstly, BAPN (0.4 mL, 20 mg/mL) was added to a flask. Then, $CaCl_2$ solution was obtained *via* mixing 100 mL $CaCl_2$ (1.5 mg/mL) and anhydrous ethanol, which was subsequently transferred to the BAPN-containing flask. Subsequently, the flask was sealed with plastic wrap and transferred to the dryer at 37 °C for 36 h. Thereafter, the solution was centrifuged at 8000 rpm for 10 min. Subsequently, the pellet was dispersed in anhydrous ethanol to obtain $CaCO_3$@BAPN nanoparticles. For the next step, $CaCO_3$@BAPN nanoparticles (2 mg), anhydrous ethanol (20 mL), EDTA (25 μL, 12 mg/mL) and ammonia (400 μL, 25%, *v*/*v*) were mixed and centrifuged at 400 rpm for 15 min. After that, TEOS (30 μL) was added and reacted for 15 min, followed by the addition of pure water for another 24 h of reaction. Samples were recovered *via* centrifugation at 8000 rpm for 10 min and the pellet was dispersed in anhydrous ethanol thus obtaining $CaCO_3$@-BAPN-CaSi. $CaCO_3$@BAPN-CaSi-NH_2 was synthesized through the reaction between $CaCO_3$@BAPN-CaSi and (3-aminopropyl) trimethoxysilane (10 μL) at 60 °C for 24 h. To enhance the nanoparticle stability, the appending NH_2 terminal groups were exploited for the conjugation of azido-PEG segment by mixing COOH-PEG1000-N_3 (50 mg), NHS (35 mg), EDC (40 mg) and $CaCO_3$@BAPN-CaSi-NH_2 (20 mg) at 400 rpm for 24 h, thus obtaining $CaCO_3$@BAPN-CaSi-PEG-N_3. At last, $CaCO_3$@-BAPN-CaSi-PEG-TAT was prepared by the click reaction between $CaCO_3$@BAPN-CaSi-PEG-N_3 (20 mg) and alkynylated TAT (20 mg), under the catalysis of pentahydrate copper sulfate (2 mg) and ascorbic acid (4 mg) in deionized water (10 mL) and stirred 24 h under nitrogen protection, and the $CaCO_3$@BAPN-CaSi-PEG-TAT was eventually recovered obtained by centrifugation. The sequence of TAT was YGRKKRRQRRR.

2.20. Evaluation of blood−brain barrier (BBB) integrity via Evans blue (EB) assay

The integrity of BBB after treatment with different nanoparticles was investigated using EB assay[40]. Nude mice were implemented according to the previous investigation[41] as the animal model primarily due to the absence of body hair, which is beneficial for monitoring the BBB integrity *via* EB assay. Meanwhile, the BBB

structure of nude mice has no significant difference with normal immunocompetent mice, which would not interfere with the analysis results[42]. Briefly, animals were first treated with different nanoparticles and then intravenously injected with EB (0.2% *w/v*, 2 mL/kg). Mice in the positive control group were injected with EB and mannitol (20%, 5 mL/kg), a commonly used BBB-opening agent[43]. Mice in the negative control group received only saline. After injection for 2 h, mouse brains were carefully dissected and EB fluorescence intensity was analyzed using the imaging system.

2.21. Fluorescence imaging and analysis of drug distribution

An IVIS Lumina III Spectrum Imaging System was used to evaluate the brain targeting effect of the nanoparticles using Cy5 as the probe. The process of Cy5 labeling was elaborated as follows. Cy5 (8 mg), 1-(3-dimethylaminopropyl)-3-ethylcarbodiimide hydrochloride (25 mg) and *N*-hydroxy succinimide (20 mg) were altogether dissolved with water in 20 mL round-bottom flask and subsequently stirred for 6 h at room temperature to activate the carboxyl groups. Thereafter, the mixture was reacted with $CaCO_3$@BAPN-CaSi-PEG-TAT for 24 h. Finally, Cy5-labeled $CaCO_3$@BAPN-CaSi-PEG-TAT ($CaCO_3$@BAPN-CaSi-PEG-TAT-Cy5) was collected *via* centrifugation. Mice were administered with either $CaCO_3$@BAPN-CaSi-PEG-TAT-Cy5 (100 μL, Cy5 dose 0.5 mg/mL) or Cy5-labeled $CaCO_3$@BAPN-CaSi ($CaCO_3$@BAPN-CaSi-Cy5) *via* tail vein. *In vivo* fluorescence images were captured after anesthesia. Finally, mice from different groups were subjected to brain dissection for further analysis.

2.22. Data analysis

The data analysis was performed *via* GraphPad 9.0 software in a blinded manner. The data was first analyzed using Shapiro−Wilk test to determine whether the results follow normal distribution. Statistical analysis methods for normally distributed data included: one-way ANOVA or repeated measure (RM)-two-way ANOVA with Tukey's test, and Brown-Forsythe ANOVA test followed by Dunnett's T3 multiple comparisons or Unpaired *t*-test with Welch's correction. For non-normally distributed data, it was analyzed using Mann Whitney U test or Kruskal−Wallis test. The summary of statistical tests was presented in Supporting Information Fig. S4. All statistical data was expressed as the mean ± SEM. *P* value below 0.05 was considered statistically significant.

3. Results

3.1. Pharmacological inhibition of LysOX attenuates seizure-induced neuronal damage in mice

Firstly, we explored whether LysOX was altered in the hippocampus after seizures. The seizure model was prepared *via* intrahippocampal injection of KA in mice as shown in Fig. 1A. The mRNA and protein expression levels of LysOX and its enzymatic activity obviously increased in the hippocampus of KA-induced seizure mouse model (Fig. 1B−E). Furthermore, LysOX evidently colocalized with the specific neuronal marker NeuN, which indicates that neuronal LysOX expression is elevated in mice post seizures (Fig. 1F). To further investigate the contribution of LysOX to neuronal damage, we inhibited the enzymatic activity of LysOX pharmacologically *via* treatment with BAPN, a previously reported irreversible LysOX inhibitor[44], as shown in Fig. 1G. The results of Nissl staining indicated that BAPN remarkably increased viable neurons in hippocampal CA1 and CA3 regions (Fig. 1H and I) while reducing the amount of locoregional degenerated neurons by FJB analysis (Fig. 1J and K). These results suggest that pharmacological blockade of LysOX can efficiently alleviate seizure-induced neuronal damage.

3.2. Deletion of LysOX in mice abrogates neuronal ferroptosis post seizures

To confirm whether the increased LysOX level is an important contributor to seizure-induced neuronal damage, neuron-specific *LysOX* KO mice were created. The diagram for generating neuron-specific *LysOX* KO mice was shown in Fig. 2A. The validation of LysOX deficiency was conducted *via* immunofluorescence (Fig. 2B) and Western blot assay (Supporting Information Fig. S5). The body weight of *LysOX* KO mice relative to the wild-type group as well as C57BL/6J normal groups was further monitored. The results demonstrated that there was no significant difference between female or male mice, indicating that the impact of neuron-specific deletion of *LysOX* on mouse growth is negligible (Fig. 2C). Consistent with the results shown above, *LysOX* KO mice were less susceptible to KA-induced seizure-like neuronal damage according to the Nissl staining results (Fig. 2D and E) and FJB analysis (Fig. 2F and G). Considering various cell death events including apoptosis, autophagy and ferroptosis (Supporting Information Fig. S6) occur in seizure mouse model triggered by KA[11], it is important to determine whether deletion of *LysOX* in neurons affects these cell death modalities. Immunoblot assay was conducted to analyze the biomarkers of apoptosis, autophagy and ferroptosis that are cleaved caspase-3, LC3II/I and GPX4, respectively. It was noteworthy that neuron-specific deletion of *LysOX* inhibited ferroptosis (shown by increased GPX4 expression) while apoptotic cascade and autophagy were not affected in *LysOX* KO mice subjected to KA (Fig. 2H). Besides, other ferroptotic indices including LPO level and *Ptgs2* mRNA were also dramatically decreased in *LysOX* KO mice after treatment with KA compared with wild-type mice injected with KA (Fig. 2I and J). These results suggest that neuron-specific deletion of *LysOX* in mice abrogates ferroptosis in KA-induced seizures.

3.3. AAV-mediated LysOX overexpression exacerbates ferroptosis-related neuronal injury post seizures

Given the positive role of LysOX for neuronal damage in seizure, we further probed whether neuronal overexpression of *LysOX* could exacerbate this effect. LysOX-expressing AAV-PHP.eB was utilized for the targeted delivery of LysOX to hippocampus. The scheme was summarized in Fig. 3A. The AAV virus successfully transferred into neurons evidenced by strong co-localization of GFP and NeuN (Fig. 3B). Overexpression of LysOX protein was confirmed by immunoblot analysis (Fig. 3C). In our preliminary experiment, *LysOX* overexpression did not evoke seizure-related neuronal damage in mice of the control group (data not shown). However, combinational treatment with sub-convulsive dose of KA (100 ng/μL) and infusion of recombinant AAV-*LysOX* rendered the mice more susceptible to ferroptosis, as shown by the elevated MDA and LPO levels (Fig. 3D). Also, the combinational treatment schedule resulted in decreasing viable neurons, which could be reversed by the ferroptosis inhibitor Lip-1 (Fig. 3E).

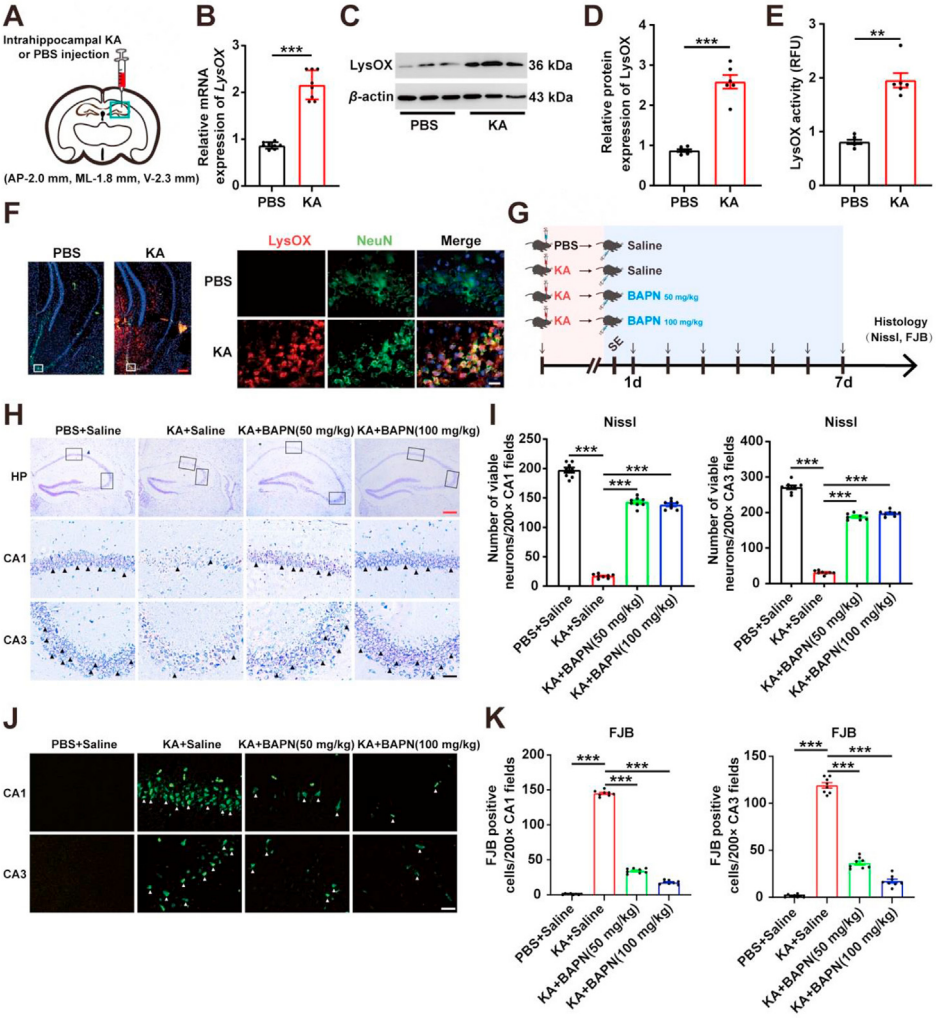

Figure 1 Inhibiting LysOX alleviates seizure-induced neuronal injury in KA-treated mouse model. (A) Schematic illustration of intra-hippocampal KA injection for seizure induction. (B−E) Alterations of LysOX in seizure mouse model at mRNA and protein levels together with its enzymatic activity ($n = 8$). (F) Colocalization of LysOX and the specific neuronal marker NeuN by immunofluorescence method. Nuclei were stained with DAPI. The red scale bar indicated 100 μm; black scale bar indicated 50 μm. (G) Schematic of BAPN treatment regimen. (H) Representative images by Nissl staining in the hippocampus of seizure mouse model when treatment with BAPN. Arrows point to Nissl positive cells. Red scale bar indicated 200 μm; black scale bar indicated 50 μm. (I) Statistical analysis of Nissl staining results in hippocampal CA1 and CA3 subregions ($n = 8$). (J) Representative images by FJB staining in the hippocampus of KA-induced seizure mouse model when treatment with BAPN. Arrows indicate FJB positive cells. Scale bar represents 25 μm. (K) Statistical analysis of FJB staining results in hippocampal CA1 and CA3 subregions ($n = 8$). All data were presented as mean ± SEM. $^{**}P < 0.01$, $^{***}P < 0.001$.

These findings again imply that LysOX contributes to ferroptotic cell death in neurons post seizures.

3.4. *LysOX activates neuronal ferroptosis via ERK-dependent phosphorylation of Alox5 in vitro*

Next, we deciphered the mechanism of LysOX-induced neuronal ferroptosis using ferroptotic cell death model in HT22 cells following glutamate (Supporting Information Fig. S7) or erastin exposure. In these two models, LysOX increased remarkably at designated time points and was positively correlated to the mRNA, protein and enzymatic activity levels (Fig. 4A−C). After knockdown of *LysOX* (Fig. 4D) by genetic silencing, glutamate- or erastin-induced neuronal death were obviously impeded (Fig. 4E and F). It was also obvious that genetic silencing of LysOX abrogated GSH depletion and accumulation of lipid ROS in these two ferroptotic cell death models (Fig. 4G). Other members of LysOX family (Loxl1, Loxl3, Loxl4) were not altered during glutamate toxicity (Supporting Information Fig. S8) while Loxl2 mRNA was undetectable (data not shown). These results support that LysOX is critical for promoting neuronal ferroptosis following glutamate challenge. Previous work showed that LysOX could enhance oxidative stress in vascular walls *via* activating p38 MAPK[45], indicating MAPK cascade as a downstream signaling for LysOX. Therefore, we further explored whether MAPK cascades were involved in the pro-ferroptosis activity of LysOX. Under glutamate exposure, LysOX blockade by gene silence or the non-toxic dose of the inhibitor BAPN (1 mmol/L, Supporting Information Fig. S9) both obviously obviated ERK phosphorylation while the phosphorylated levels of JNK and p38 were not

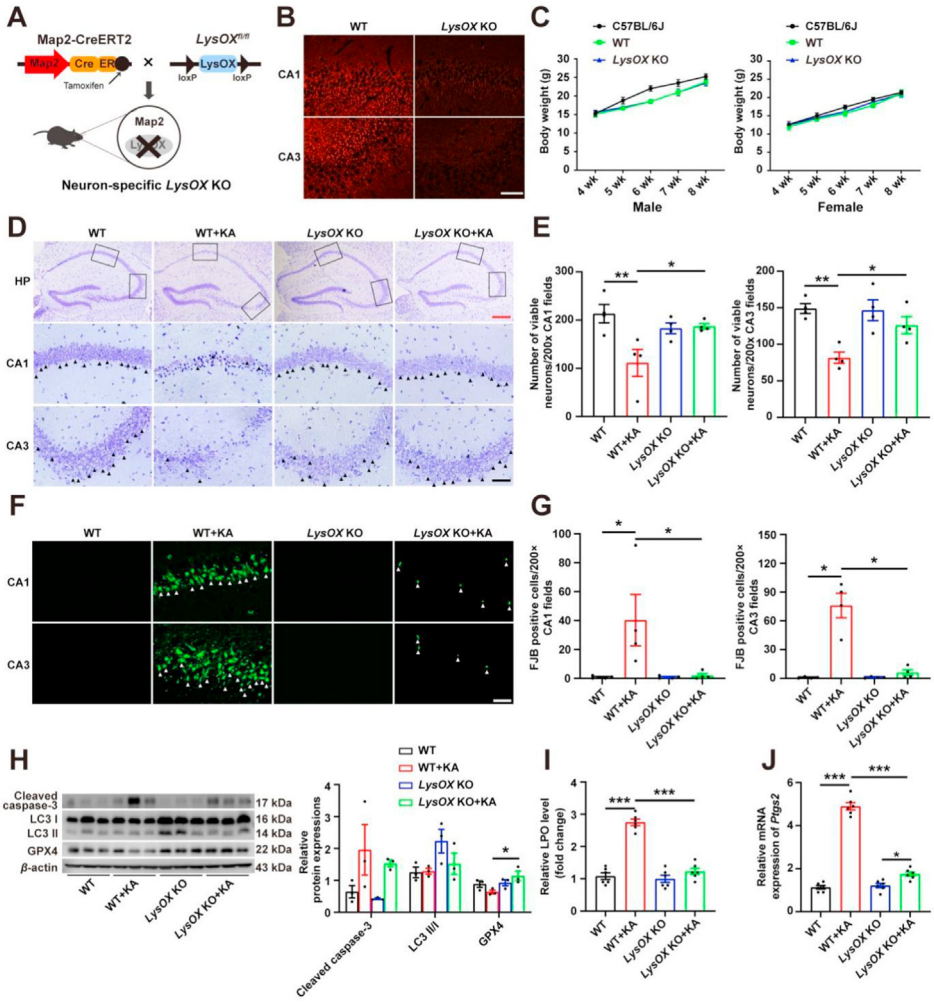

Figure 2 Neuron-specific *LysOX* deletion obviates ferroptosis-related injury in seizure mouse model. (A) Schematic diagram of *LysOX* knockout (KO) mice. (B) Validation of deletion of *LysOX* by immunofluorescence. (C) Body weight changes of *LysOX* KO, wild type (WT) and normal (C57BL/6J) mice at 4, 5, 6, 7 and 8 weeks ($n = 8$). (D) Representative images by Nissl staining in the hippocampus of KA-treated *LysOX* KO mice. Arrows indicate Nissl positive cells. Red scale bar indicates 200 μm; black scale bar indicates 50 μm. (E) Statistical analysis of Nissl staining results in hippocampal CA1 and CA3 subregions ($n = 3$). (F) Representative images by FJB staining in the hippocampus of KA-treated *LysOX* KO mice. Arrows indicate FJB positive cells. Scale bar indicates 25 μm. (G) Quantitation of FJB staining results in hippocampal CA1 and CA3 subregions ($n = 3$). (H) Effects of *LysOX* KO on the indices of apoptosis (cleaved caspase-3), autophagy (LC3II/I) and ferroptosis (GPX4) in mice subjected to KA by Western blot analysis ($n = 3$). (I) and (J) Effects of *LysOX* KO on other ferroptosis indices including LPO and *Ptgs2* in mice subjected to KA ($n = 6$). All the data were shown as mean ± SEM. $^{**}P < 0.01$, $^{***}P < 0.001$.

affected (Fig. 4H, Supporting Information Fig. S10). Inhibition of LysOX also resulted in elevation of GPX4 following glutamate challenge, which further confirms that LysOX promotes neuronal ferroptosis. It was also interesting to note that ERK inhibitor U0126 did not affect LysOX expression, but decreased Alox5 phosphorylation at Ser663 (Fig. 4I). Consistently, ERK inhibitor U0126 or Alox5 inhibitor Zileuton obviously abrogated oxidative glutamate toxicity in neurons (Supporting Information Fig. S11A–C) and inhibited ferroptosis (including cumulative lipid ROS and *Ptgs2* mRNA)[46,47] (Fig. S11D–G). We also validated the protective effect of ERK inhibition against erastin-induced neuronal ferroptosis (Supporting Information Fig. S12). In contrast, inhibition of either p38 (SB203580) or JNK (SP600125) did not prevent neuron death (Fig. S12). Collectively, these results implicate that LysOX contributes to ferroptotic events likely *via* activating ERK-Alox5 signaling.

3.5. *AAV-LysOX promotes ERK-dependent Alox5 phosphorylation in mouse seizure model*

Next, we investigated whether ERK-dependent Alox5 phosphorylation is involved in the deleterious effect of LysOX on ferroptosis-related neuronal injury in mouse with KA-induced seizure. The experimental diagram was indicated in Fig. 5A. LysOX overexpression *in vivo* increased the phosphorylation levels of ERK and Alox5 (Ser663) under a sub-convulsive dose of 100 ng/μL KA (Fig. 5B and C), while no evident alteration of activated ERK and Alox5 was found in 100 ng/μL KA-treated group compared with matched control. We assumed that the sub-convulsive dose of KA (100 ng/μL) did not trigger ferroptosis as our previous publications and other research group have depicted that neuronal death pathways are rarely activated without epileptic seizures[11,48]. Additionally, following treatments with the

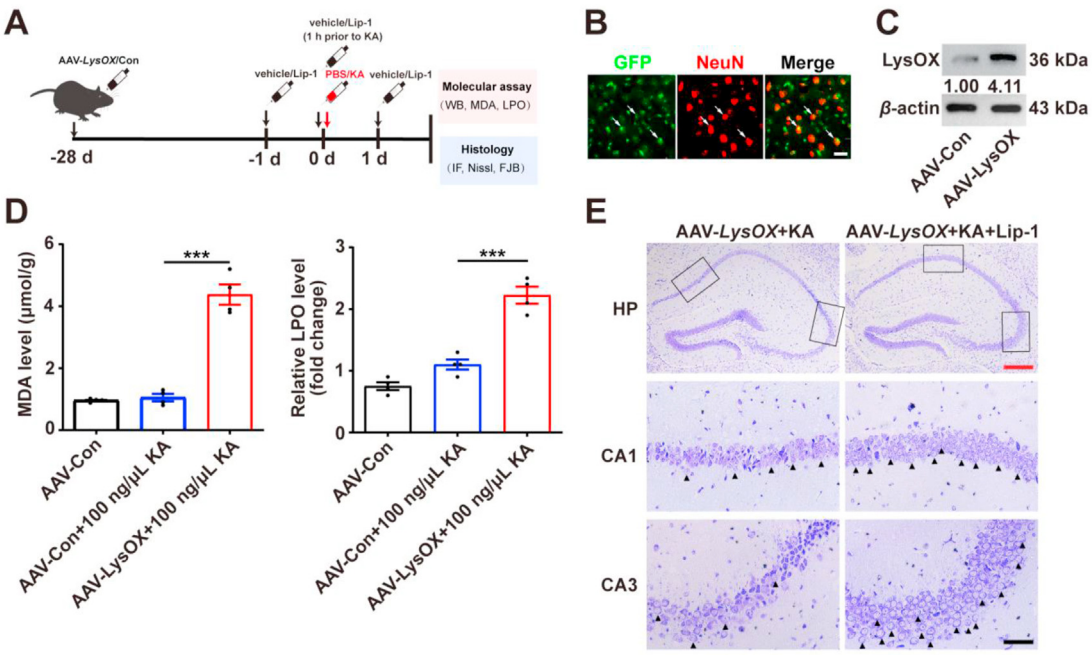

Figure 3 AAV-mediated *LysOX* overexpression exacerbates ferroptosis-related injury after seizures. (A) Experimental regimen for AAV-mediated *LysOX* transfer and Lip-1 treatment. (B) Representative images showing neuronal distribution of virus in the hippocampus. Scale bar indicated 50 μm. (C) Representative protein bands indicating LysOX overexpression in hippocampus upon AAV-PHP.eB injection. Ratios are normalized to β-actin (loading control). (D) Effects of LysOX overexpression on MDA and LPO levels in mice after seizures ($n = 4$). (E) Effects of Lip-1 on the survival of ferroptotic neurons induced by combination with AAV-mediated *LysOX* transfer and subconvulsive dose (100 ng/μL) of KA. Red scale bar and black scale bar indicate 200 and 50 μm, respectively. All data were expressed as mean ± SEM. ***$P < 0.001$.

sub-convulsive dose of KA (100 ng/μL) and the ERK inhibitor U0126, the phosphorylation level of Alox5 was significantly suppressed, accompanied with inhibited ferroptosis indices (LPO and MDA) and neuronal injury (Nissl staining results) in mice undergone LysOX overexpression (Fig. 5D–F). Treatment with the specific Alox5 inhibitor Zileuton also prevented ferroptosis and neuronal impairment in mice with sub-convulsive dose of KA (100 ng/μL) and recombinant LysOX overexpression (Fig. 5E–G). Collectively, the observations showed ERK-Alox5 acts as the downstream signaling events underlying the LysOX-mediated ferroptotic neuronal injury.

3.6. *Characterization of $CaCO_3$@BAPN-CaSi-PEG-TAT*

Clinical translation of the LysOX inhibitor BAPN has long been impeded by its cardiotoxicity[49] and neurotoxicity[50]. The construction of ferroptosis-ameliorating nanoformulation for attenuating seizure-induced neuronal damage is illustrated in Fig. 6A. The COOH-PEG-N_3 and alkynylated TAT ligands were firstly synthesized and characterized by NMR (Supporting Information Fig. S13A), of which the results not only confirmed their successful preparation but also suggested their high purity. Meanwhile, BAPN-incorporated $CaCO_3$-based nanocores ($CaCO_3$@BAPN) were prepared through the gas-diffusion-enabled co-condensation of BAPN and Ca^{2+} ions under atmospheric CO_2. A thin layer of Ca-Si hybrid was then deposited onto the $CaCO_3$@BAPN substrates ($CaCO_3$@BAPN-CaSi), which exerts facile control over the ion exchange between the core and solution medium while also potentiating further surface modification. Eventually, the PEG ligand and cell-penetrating TAT peptides were sequentially modified onto the CaSi shell as the outermost layer *via* amide reaction and click reaction ($CaCO_3$@BAPN-CaSi-PEG-TAT) to endow enhanced blood circulation stability and BBB penetration capability. To explore the structural and morphological features of the nanoformulations, the samples series were visualized *via* SEM and TEM. As shown in Fig. 6B and C, the $CaCO_3$@BAPN nanocores were highly monodispersive with a uniform spherical morphology, presenting the diameter of approximately 90 nm according to statistical analysis. The stepwise preparation of $CaCO_3$@BAPN-CaSi-PEG-TAT was supported by the zeta potential analysis (Fig. S13B), for which the $CaCO_3$@BAPN-CaSi showed a highly positive surface charge of around 20 mV but turned negative after the grafting of PEG-TAT ligands. Interestingly, high-resolution TEM, selected area electron diffraction and powder X-ray diffraction analysis collectively demonstrated the noncrystalline nature of the eventual $CaCO_3$@BAPN-CaSi-PEG-TAT product in Fig. 6D, E and H, indicating that the amorphous feature of the $CaCO_3$-based nanosystem generated through gas-diffusion-dependent co-condensation has been maintained throughout the preparation process. Energy-dispersive X-ray spectroscopy of the $CaCO_3$@BAPN-CaSi-PEG-TAT nanosystem showed that the BAPN molecules were homogenously embedded in the $CaCO_3$ matrix (Fig. 6F). The nanoparticle monodispersity and shape were well maintained after the deposition of CaSi shell and PEG-TAT peptides (Fig. S13C), of which the diameter eventually increased to around 100 nm. The changes in nanoparticle sizes were also consistently supported by the DLS analysis (Fig. 6G), which revealed a slight increase in hydrodynamic diameter from 90 nm of $CaCO_3$@BAPN to 100 nm of $CaCO_3$@BAPN-CaSi-PEG-TAT.

The graft rate of PEG in nanoparticles was assessed by two methods including thermogravimetric analysis and fluorescence

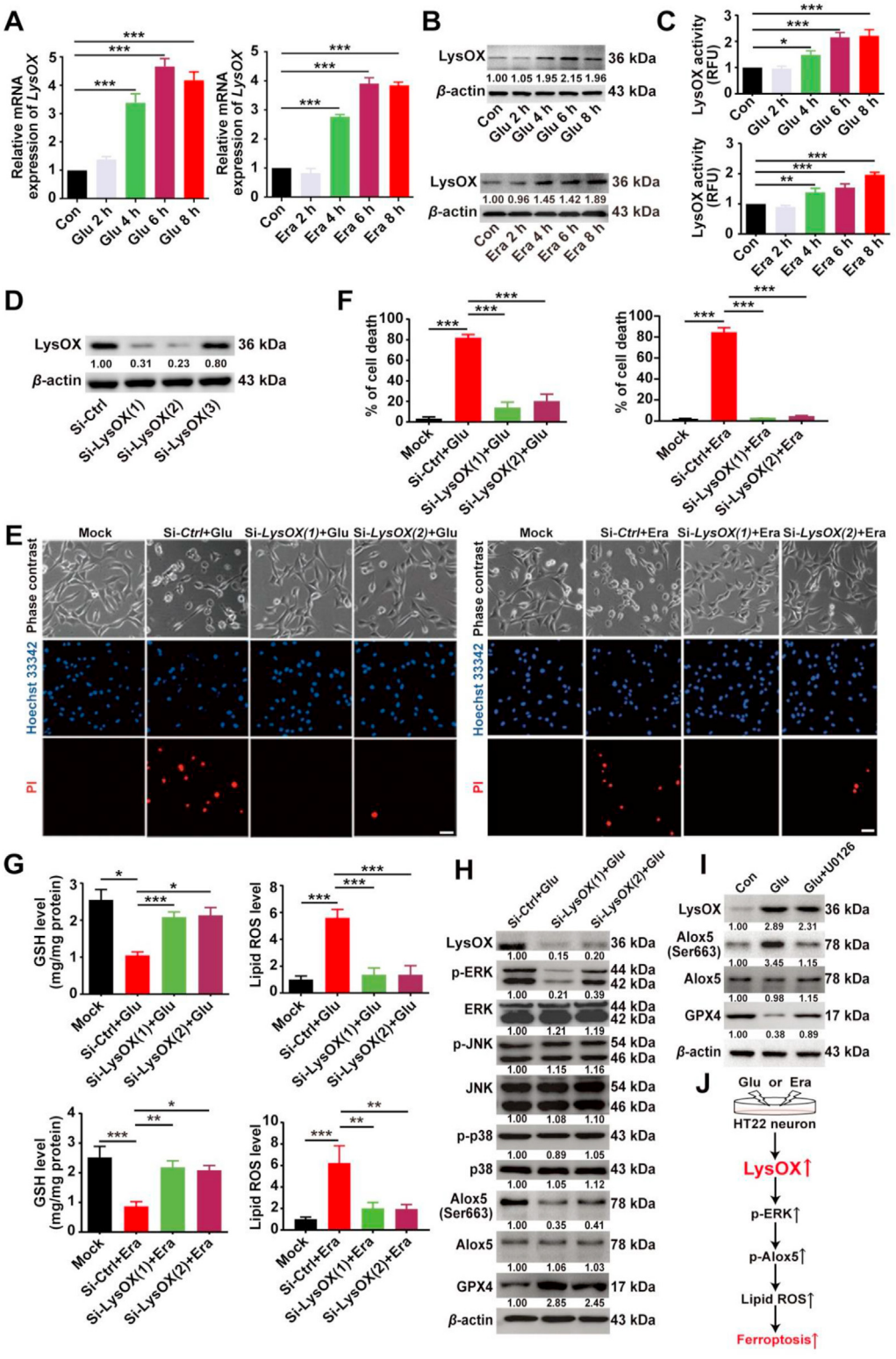

Figure 4 LysOX triggers ferroptosis process *via* ERK-dependent phosphorylation of Alox5 *in vitro*. (A–C) Alterations of LysOX at mRNA and protein expressions as well as enzyme activities at designated time points (2, 4, 6 and 8 h) RT-qPCR and enzymatic activity detections, $n = 3$. (D) Validation of *LysOX* knock down (KD) in HT22 neuronal cells by Western blot analysis. (E) Representative images showing the effects of *LysOX* KD on neuronal death in Glu- or Era-induced ferroptosis in HT22 neuronal cells *via* PI/Hoechst 33342 staining. Scale bar indicated 100 μm. (F) Analysis of cell death rate *via* flow cytometry in Glu- or Era-induced ferroptosis after *LysOX* KD in HT22 cells ($n = 3$). (G) Effects of *LysOX* KD on GSH and lipid ROS levels in Glu- or Era-treated H22 cells ($n = 3$). (H) Effects of *LysOX* KD on the protein levels of MAPK cascades (ERK, JNK and p38), Alox5 and GPX4 in Glu-treated HT22 cells. (I) Alterations of the protein expressions of Alox5 and GPX4 in Glu-treated HT22 cells when treatment with ERK inhibitor U0126. (J) Schematic depiction of ERK-Alox5 axis as the downstream signaling event of LysOX in Glu-induced neuronal ferroptosis. All the results were presented as mean ± SEM. $^{*}P < 0.05$, $^{**}P < 0.01$, $^{***}P < 0.001$.

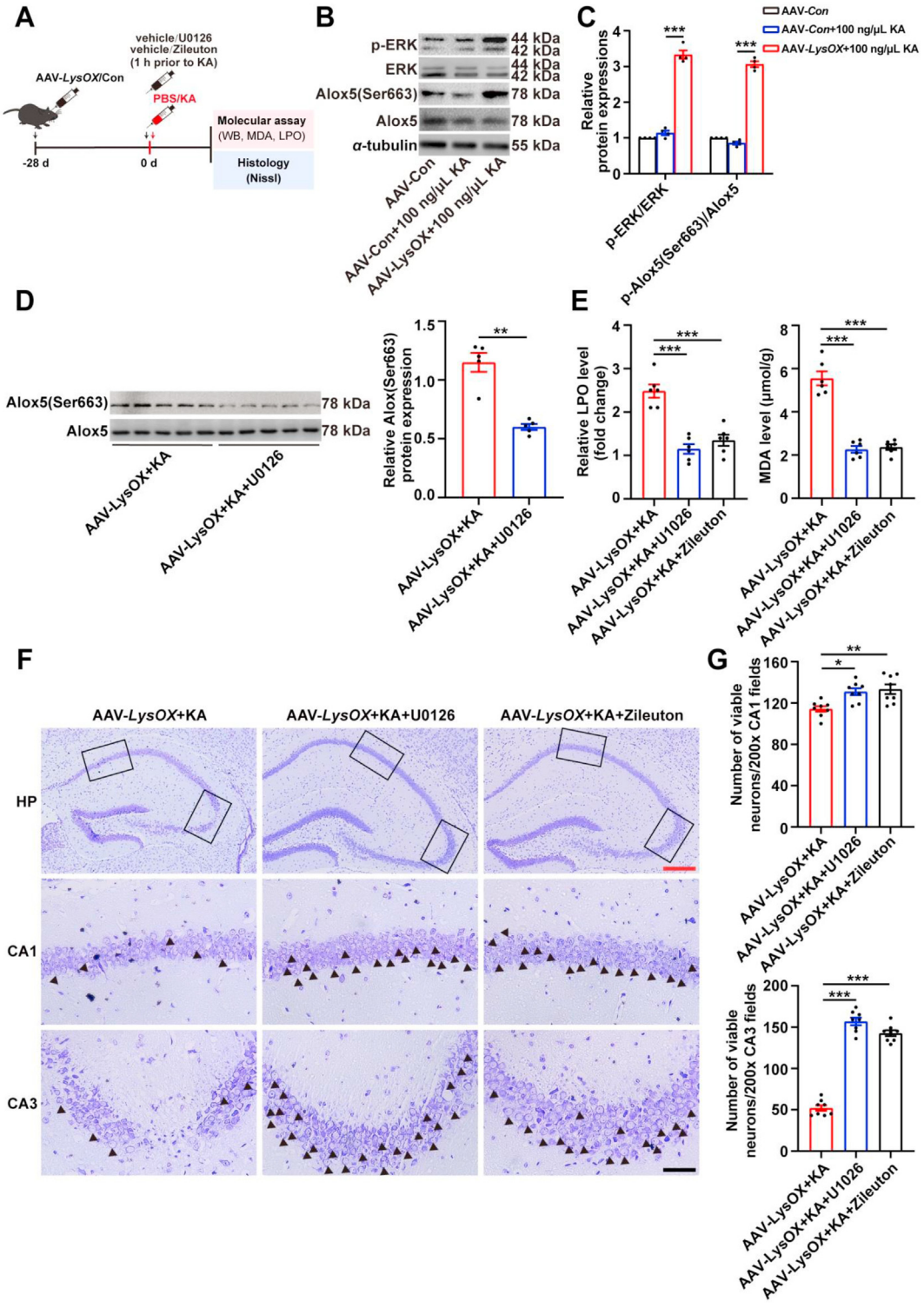

Figure 5 AAV-LysOX promotes ERK activation and Alox5 phosphorylation in KA-treated seizure mouse models. (A) Experimental procedure. (B) LysOX overexpression augmented ERK phosphorylation (Thr202/Tyr204 residue) and Alox5 phosphorylation (Ser663 residue). (C) Statistical analysis ($n = 4$). (D) Effects of U0126 on the phosphorylated Alox5 protein expression and its total form in mice subjected to AAV-*LysOX* and subconvulsive dose (100 ng/μL) of KA ($n = 5$). (E) Effects of Alox5 inhibitor Zileuton or ERK inhibitor U0126 on LPO and MDA levels in mice subjected to AAV-*LysOX* and subconvulsive dose (100 ng/μL) of KA ($n = 6$). (F) Effects of Zileuton or U0126 on the neuronal viability in mice subjected to AAV-*LysOX* and sub-convulsive dose (100 ng/μL) of KA by Nissl staining. (G) Statistical analysis of Nissl staining results ($n = 8$). Red scale bar and black scale bar indicate 200 μm and 50 μm, respectively. All data were expressed as mean ± SEM. $^{**}P < 0.01$, $^{***}P < 0.001$.

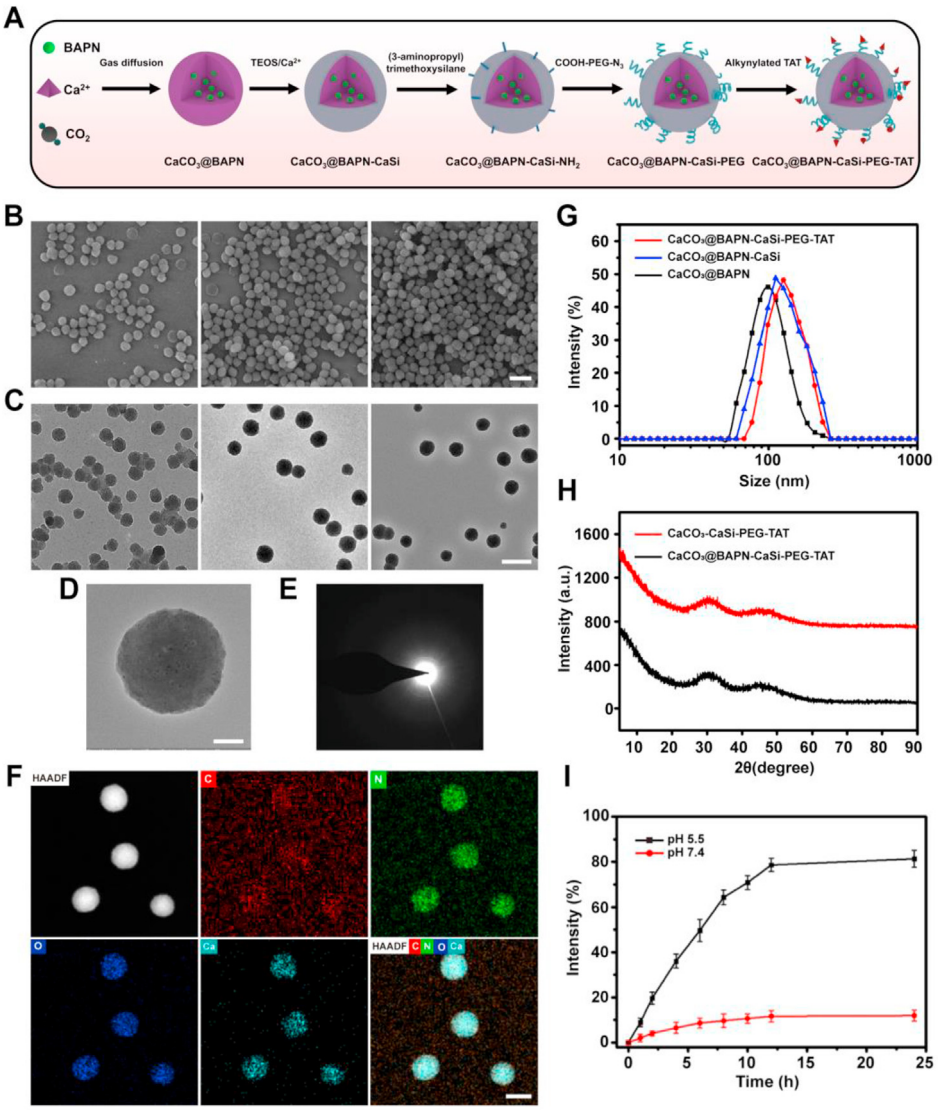

Figure 6 Characterization of $CaCO_3$@BAPN-CaSi-PEG-TAT. (A) Schematic illustration of the synthesis procedures for $CaCO_3$@BAPN-CaSi-PEG-TAT. (B) SEM images of $CaCO_3$@BAPN, $CaCO_3$@BAPN-CaSi and $CaCO_3$@BAPN-CaSi-PEG-TAT. Scale bar indicated 300 nm. (C) Transmission electron microscopic (TEM) images of $CaCO_3$@BAPN, $CaCO_3$@BAPN-CaSi and $CaCO_3$@BAPN-CaSi-PEG-TAT. Scale bar indicated 200 nm. (D) High-resolution TEM images of $CaCO_3$@BAPN-CaSi-PEG-TAT. Scale bar indicated 25 nm. (E) Selected area electron diffraction pattern of $CaCO_3$@BAPN-CaSi-PEG-TAT. (F) HAADF-STEM images of $CaCO_3$@BAPN-CaSi-PEG-TAT and the corresponding elemental mapping results. Scale bar indicated 100 nm. (G) DLS-based size distribution analysis of $CaCO_3$@BAPN, $CaCO_3$@BAPN-CaSi and $CaCO_3$@BAPN-CaSi-PEG-TAT in aqueous media. (H) Powder X-ray diffraction analysis of $CaCO_3$-CaSi-PEG-TAT (a control system) and $CaCO_3$@BAPN-CaSi-PEG-TAT. (I) HPLC-based analysis on the time-dependent BAPN release under pH = 7.4 and 5.5.

spectrophotometer. As indicated in Fig. S13D, the relative weight ratio of PEG in PEGylated $CaCO_3$@BAPN-CaSi-PEG was around 8.1%, while the weight ratio of TAT in the $CaCO_3$@BAPN-CaSi-PEG-TAT was 11.9%. It was also noted that the graft rate of PEG was approximately 8.3% according to the quantification by fluorescence spectrophotometer (Fig. S13E). These results indicate that PEG in PEGylated nanoparticles has been successfully modified. According to the HPLC analysis in Fig. S13F, the loading amount of BAPN in the final product was around 5%. Taking advantage of the amorphous nature of $CaCO_3$ and the release control mechanism of the CaSi shell, the BAPN leakage at neutral pH of 7.4 was almost negligible, which was around 10% after 24 h of incubation (Fig. 6I). However, BAPN release rate increased rapidly under the acidic pH of 5.5 that resembled the lysosomal microenvironment[51] and the accumulative release ratio reached above 80% within 12 h. As collectively demonstrated by the results above, the $CaCO_3$@BAPN-CaSi-PEG-TAT nanoparticles could effectively encapsulate BAPN molecules and release them in a bioresponsive manner, which is crucial for reducing their systemic toxicity while maximize the therapeutic index.

3.7. $CaCO_3$@BAPN-CaSi-PEG-TAT efficiently targets the brain and has no toxicity

The safety of the $CaCO_3$@BAPN-CaSi-PEG-TAT nano-formulation was further studied *in vivo*. To start with, we firstly investigated the pharmacokinetic and biosafety characteristics of the $CaCO_3$@BAPN-CaSi-PEG-TAT nanoformulation after systemic

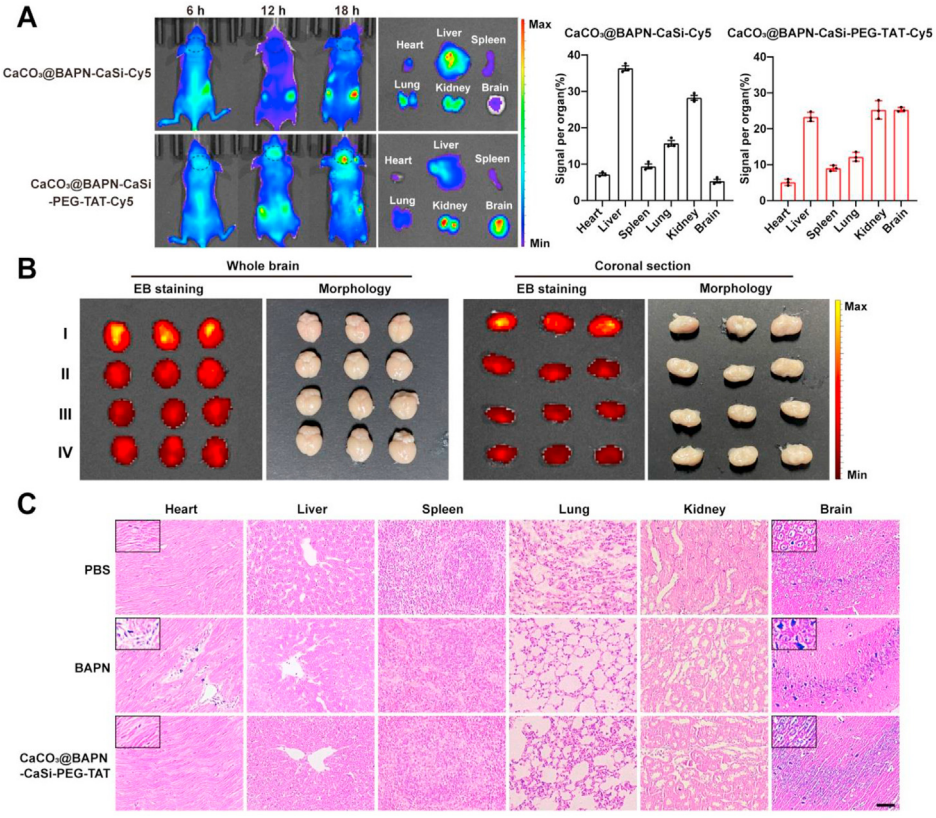

Figure 7 $CaCO_3$@BAPN-CaSi-PEG-TAT efficiently target to the brain and has no toxicity. (A) *In vivo* whole-body imaging showing the time-dependent systemic distribution of $CaCO_3$@BAPN-CaSi-Cy5 and $CaCO_3$@BAPN-CaSi-PEG-TAT-Cy5 post intravenous injection. (B) Evans blue assay on the BBB integrity in mice after treatment with I: mannitol; II: PBS; III: $CaCO_3$-CaSi-PEG-TAT; IV: $CaCO_3$@BAPN-CaSi-PEG-TAT, respectively. (C) Histological inspections on major mouse organs *via* H&E staining after different treatments. Scale bar indicates 100 μm.

administration. Here the nanoparticles were labeled with a near infrared dye Cy5 during co-condensation to allow *in vivo* tracking. After the intravenous injection through the tail vein, the non-neuron-targetable $CaCO_3$@BAPN-CaSi-Cy5 were primarily accumulated in the mouse liver, lungs and kidneys, which could be explained by the intrinsic susceptibility to the mononuclear phagocyte system-mediated nanoparticle clearance due to the lack of anti-opsonization PEG ligands. More importantly, the fluorescence deposition in the brain was almost negligible, again necessitating the integration of BBB-penetrating strategies. In contrast, mouse brain in the $CaCO_3$@BAPN-CaSi-PEG-TAT-Cy5 group showed increasing Cy5 fluorescence in a time-dependent manner, while the Cy5 fluorescence deposition in those non-specific organs substantially decreased. The *in vivo* fluorescence imaging results were further quantitatively investigated, which revealed that the relative brain drug deposition in the $CaCO_3$@-BAPN-CaSi-PEG-TAT-Cy5 group has increased by 20% compared to the $CaCO_3$@BAPN-CaSi-Cy5 group (Fig. 7A). After confirming the superior brain-targeted BAPN delivery capability of $CaCO_3$@BAPN-CaSi-PEG-TAT nanoformulation, we further investigated its biosafety *via* multiple techniques. Specifically, histological inspections and EB staining of the extracted brain tissues showed that the tissue damage amount of necrotic neurons after the treatment of $CaCO_3$@BAPN-CaSi-PEG-TAT was almost negligible, whereas brain samples in the mannitol group (a common BBB-opening agent) have become yellow due to BBB disruption with large amounts of necrotic neurons, showing that the $CaCO_3$@BAPN-CaSi-PEG-TAT nanoformulation could traverse the BBB in a safe and non-invasive manner by exploiting the BBB-penetrating capability of the TAT ligands (Fig. 7B). Furthermore, hematoxylin and eosin (H&E) staining of the extracted major mouse organs showed that the $CaCO_3$@BAPN-CaSi-PEG-TAT formulation has substantially alleviated the cardiotoxic and neurotoxic effects of BAPN, evidenced by the almost identical histological patterns in the PBS and $CaCO_3$@BAPN-CaSi-PEG-TAT groups (Fig. 7C). These results confirmed that the $CaCO_3$@BAPN-CaSi-PEG-TAT nanoformulation could be exploited as a safe and effective BAPN carrier.

4. Discussion

Seizures have long been postulated as a common symptom in a plethora of neuropsychiatric diseases notable in epilepsy. Repetitive seizures could trigger neuronal damage and neurodegeneration[52], finally exacerbating epileptic progression. Cell death has been demonstrated to act as the key event in seizure-induced neuronal damage[11]. However, the regulatory role and mechanism of cell death in neuronal damage post seizures are not clearly characterized. Recently, ferroptosis is a newly discovered cell death closely related to various neurologic conditions[15]. Our previous studies revealed the characteristic changes of ferroptosis in a variety of seizure models[17,18]. Here, we further explored the ferroptosis regulatory network in seizures and identified LysOX as a novel ferroptosis factor promoting neuronal ferroptosis and

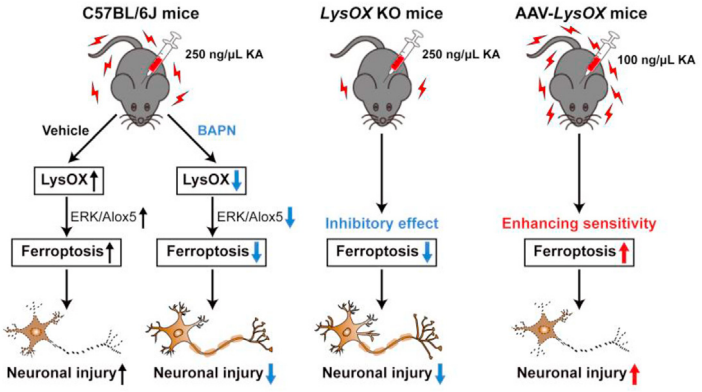

Figure 8 Scheme model illustrating LysOX promotes ferroptosis and exacerbates seizure-induced neuronal damage. ERK-dependent Alox5 phosphorylation is involved in the contribution of LysOX to ferroptosis-related neuronal injury after seizures.

aggravating seizure-induced neuronal injury. Mechanistically, we also identified ERK-Alox5 axis as downstream signaling of LysOX for the promotion of ferroptosis-associated lipid peroxidation (Fig. 8). The results that LysOX inhibition alleviated ferroptosis and ameliorated seizure-induced neuronal damage indicate its promising therapeutic potential.

LysOX is an endogenous amino oxidase that catalyzes collagen crosslinking[21]. Nowadays, experimental results support that LysOX family possesses important biological functions. LysOX is an identified contributor in cancer migration, adhesion and metastasis[53,54]. Inhibition of LysOX in tumor cells by BAPN or CCT365623 suppresses their malignancy[54,55]. Moreover, LysOX also exacerbates Alzheimer's disease and spinal cord injury[26,56]. Additionally, increased nuclear localization of LysOX propeptide can also result in abnormal neuronal development of Purkinje cell dendrites[57]. However, the detailed function of LysOX in seizure-related neuronal injury remains unknown. Our present work provides the first evidence showing pro-ferroptosis feature of LysOX amplifies seizure-induced neuronal damage. The deleterious effects of LysOX can be reversed by BAPN treatment.

Our findings also provide the molecular mechanism that LysOX promotes neuronal ferroptosis. We prove that ERK-dependent Alox5 phophorylation is essential for the promotion of LysOX to neuronal ferroptosis following exposure to glutamate, an analog of KA. Prior work reported LysOX level is positively correlated to vascular oxidative stress (a vital ferroptosis marker) in hypertensive rodent model[45], which partially supported pro-ferroptosis effect of LysOX. In contrast to p38 activation after LysOX overexpression in hypertension, our current work reveals no significant effect of p38 following LysOX inhibition in neuronal ferroptotic cell death models. This interesting discrepancy is attributed to different stressors. Under glutamate or erastin-induced neuronal ferroptosis, ERK was inactivated after LysOX inhibition. Previous investigations show the dual roles of ERK with both protective and detrimental actions. ERK activation may suppress neuronal apoptosis but facilitate necrotic death process[58]. It is tempting to extrapolate that ERK activation is involved in triggering ferroptosis. The evidence for the contribution of ERK in ferroptotic cell death arises from the previous study showing that ERK inhibition by U0126 blocks erastin-induced ferroptosis in cancer cells[15].

Meanwhile, ERK causes Alox5 phosphorylation at Ser663 residue and subsequently increase Alox5 activity in leukocytes[59], suggesting that ERK is critical for Alox5 activation. Alox5 is one of the most important non-heme-iron lipoxygenases with tightly regulated cell activities[59]. It has reported that eicosapentaenoic acid, arachidonic acid and docosahexaenoic acid are substrates for Alox5, all of which are poly-unsaturated fatty acids (PUFAs) richly deposited in neuronal membrane. Catalyzation of PUFAs by Alox5 is involved in diverse biological reactions including inflammation and lipid peroxidation[60], finally causing several human diseases such as asthma and neurological disorders[61,62]. Recent studies revealed that gene knockout of Alox5 or zileuton treatment[63], rescued synaptic function and improved memory performance in a transgenic mouse model of Alzheimer's disease[64], raising the possibility that Alox5 could facilitate the pathology of this disease. Of note, oxidation of PUFAs by lipoxygenases has been implicated in the execution of ferroptotic cell death[65]. In particular, it was previously reported that Alox5 activation caused ferroptotic process in glutamate- or erastin-induced neurotoxicity[46]. Suppression of this enzyme protected neurons against glutamate- or erastin-induced cell death as well as improving prognosis of mouse models following hemorrhagic stroke[46,66]. Our current work demonstrates a marked elevation of Alox5 Ser663 phosphorylation by activation of ERK in ferroptosis. Genetic silencing or pharmacological inhibition of LysOX causes ERK-dependent abrogation of Alox5 at phosphorylated level, thereby inhibiting ferroptosis-related lipid peroxidation. These results strongly implicate that targeting LysOX-ERK-Alox5 axis is of utmost importance for the initiation and execution of neuronal ferroptosis (Fig. 8). Additionally, our present work also shows that LysOX overexpression by AAV delivery leads to phosphorylated levels of ERK and Alox5 when combination with the sub-convulsive dose of KA (100 ng/μL). It is interesting to note that, in mice treated with 100 ng/μL of KA, no evident change occurred for the phosphorylation of ERK and Alox5. A possible explanation is that the sub-convulsive dose of KA is insufficient for evoking seizure. Consistent with this hypothesis, previous investigations reveal that only repeated seizures can trigger neuronal death process[11,48].

From a translational perspective, nanotechnology-based drug delivery is employed in the present work to improve the therapeutic index of BAPN due to the associated cardiotoxicity[49] and neurotoxicity[50]. There are hitherto three main categories of nanoparticles, namely organic, inorganic and hybrid based on the chemical properties[67]. Among these nanomaterials, inorganic nanoparticles offer some advantages for the implementation of targeted drug delivery, notably in bioavailability. Great attention

has especially been grabbed in the aspect of calcium-based inorganic materials including calcium carbonate, calcium phosphate, calcium silicate and calcium fluoride, owing to their excellent biocompatible and biodegradable properties[68]. Our previous investigations have depicted that calcium carbonate is considered as good nanocarriers for drug delivery in medical science[51]. Although, results from our present work indicated $CaCO_3$@BAPN-CaSi-PEG-TAT and BAPN have the similar effects on the neuronal damage post seizure (data not shown), the mice injected with $CaCO_3$@BAPN-CaSi-PEG-TAT exhibited the normal histology in the heart and the brain while BAPN group induced pronounced necrosis in these two organs, indicating that delivery of BAPN *via* nanotechnology has potential therapeutic implications. Given that calcium carbonate-based biomaterial has been shown to be a safe and viable approach for the delivery of various drugs including insulin in healthy human volunteers[69], our present findings in rodents may have promising clinical translations for patients with seizure-associated disorders such as epilepsy.

There is also the limitation in our present work. For instance, the relationship between the contribution of LysOX to neuronal damage post seizure and epileptogenesis is not explored. And whether LysOX has any directly regulatory role in epileptic progression is also not illustrated. Further investigation is warranted to clinically testing LysOX-targeted therapeutic implication in the progress of disease pathology. In any way, due to the critical role of ferroptosis in seizure-induced neuronal damage, we believe that LysOX could serve as a promising target for alleviating seizure-related neuronal injury in various neurological conditions such as epilepsy.

5. Conclusions

In summary, our findings demonstrate that targeting ferroptosis provides a rationale for amelioration of seizure-induced neuronal damage and furthermore reveal the LysOX-ERK-Alox5 axis is an important pathway to elicit ferroptosis-associated overproduction of lethal lipid peroxide, while inhibiting LysOX in neurons could alleviate seizure-induced hippocampal damage. The currently recognized pathway is leveraged to develop a novel therapeutic approach that reduces brain damage in seizure disorder such as epilepsy.

Acknowledgments

This work was supported by the National Natural Science Foundation of China (No. 81974502 and 81671293), the Natural Science Foundation of Hunan Province (No. 2020JJ3061, China), and the Hunan Provincial Department of Education Innovation Platform Open Fund Project (No. 17K100, China).

Author contributions

Xiaoyuan Mao and Weilin Jin initiated the project. Xiaoyuan Mao, Qin Li and Jining Jia performed the experiments. Xiaoyuan Mao and Xuan Wang conducted the data analysis. Xiaoyuan Mao drafted the manuscript. Xiaoyuan Mao, Menghuan Li, Mingzhu Jin, Honghao Zhou, Zhong Luo, Yanli Zhao, Zhaoqian Liu and Weilin Jin revised the manuscript. All authors read and approved the final version of manuscript.

Conflicts of interest

The authors declare that they have no competing interests.

Appendix A. Supporting information

Supporting data to this article can be found online at https://doi.org/10.1016/j.apsb.2022.04.017.

References

1. Boursoulian LJ, Adeseye V, Malow BA, Ess K. Recurrence rate of the first nonfebrile seizure in children with autism spectrum disorder. *Epilepsy Behav* 2021;**122**:108187.
2. Mazzucchi E, Vollono C, Pauletto G, Lettieri C, Budai R, Gigli GL, et al. The persistence of seizures after tumor resection negatively affects survival in low-grade glioma patients: a clinical retrospective study. *J Neurol* 2022;**269**:2627−33.
3. Ferreira-Atuesta C, Döhler N, Erdélyi-Canavese B, Felbecker A, Siebel P, Scherrer N, et al. Seizures after ischemic stroke: a matched multicenter study. *Ann Neurol* 2021;**90**:808−20.
4. Dumanis SB, French JA, Bernard C, Worrell GA, Fureman BE. Seizure forecasting from idea to reality. Outcomes of the My seizure gauge epilepsy innovation institute workshop. *eNeuro* 2017;**4**:e0349−17.
5. Proix T, Truccolo W, Leguia MG, Tcheng TK, King-Stephens D, Rao VR, et al. Forecasting seizure risk in adults with focal epilepsy: a development and validation study. *Lancet Neurol* 2021;**20**:127−35.
6. Devinsky O, Vezzani A, O'Brien TJ, Jette N, Scheffer IE, de Curtis M, et al. Epilepsy. *Nat Rev Dis Prim* 2018;**4**:18024.
7. Farrell JS, Wolff MD, Teskey GC. Neurodegeneration and pathology in epilepsy: clinical and basic perspectives. *Adv Neurobiol* 2017;**15**:317−34.
8. Singh T, Batabyal T, Kapur J. Neuronal circuits sustaining neocortical-injury-induced status epilepticus. *Neurobiol Dis* 2022;**165**:105633.
9. Lee DA, Lee J, Kim HC, Park KM, Kim SE. Hippocampal injury in patients with status epilepticus: quantitative analysis of hippocampal volume and structural co-variance network. *Seizure* 2022;**95**:84−9.
10. Van Coillie S, Van San E, Goetschalckx I, Wiernicki B, Mukhopadhyay B, Tonnus W, et al. Targeting ferroptosis protects against experimental (multi)organ dysfunction and death. *Nat Commun* 2022;**13**:1046.
11. Mao XY, Zhou HH, Jin WL. Redox-related neuronal death and crosstalk as drug targets: focus on epilepsy. *Front Neurosci* 2019;**13**:512.
12. Badgley MA, Kremer DM, Maurer HC, DelGiorno KE, Lee HJ, Purohit V, et al. Cysteine depletion induces pancreatic tumor ferroptosis in mice. *Science* 2020;**368**:85−9.
13. Zou Y, Henry WS, Ricq EL, Graham ET, Phadnis VV, Maretich P, et al. Plasticity of ether lipids promotes ferroptosis susceptibility and evasion. *Nature* 2020;**585**:603−8.
14. Ubellacker JM, Tasdogan A, Ramesh V, Shen B, Mitchell EC, Martin-Sandoval MS, et al. Lymph protects metastasizing melanoma cells from ferroptosis. *Nature* 2020;**585**:113−8.
15. Dixon SJ, Lemberg KM, Lamprecht MR, Skouta R, Zaitsev EM, Gleason CE, et al. Ferroptosis: an iron-dependent form of non-apoptotic cell death. *Cell* 2012;**149**:1060−72.
16. Mao XY, Zhou HH, Jin WL. Ferroptosis induction in pentylenetetrazole kindling and pilocarpine-induced epileptic seizures in mice. *Front Neurosci* 2019;**13**:721.
17. Li Q, Li QQ, Jia JN, Sun QY, Zhou HH, Jin WL, et al. Baicalein exerts neuroprotective effects in $FeCl_3$-induced posttraumatic epileptic seizures *via* suppressing ferroptosis. *Front Pharmacol* 2019;**10**:638.
18. Jia JN, Yin XX, Li Q, Guan QW, Yang N, Chen KN, et al. Neuroprotective effects of the anti-cancer drug lapatinib against epileptic seizures *via* suppressing glutathione peroxidase 4-dependent ferroptosis. *Front Pharmacol* 2020;**11**:601572.

19. Chen KN, Guan QW, Yin XX, Wang ZJ, Zhou HH, Mao XY. Ferrostatin-1 obviates seizures and associated cognitive deficits in ferric chloride-induced posttraumatic epilepsy *via* suppressing ferroptosis. *Free Radic Biol Med* 2022;**179**:109−18.
20. Vallet SD, Ricard-Blum S. Lysyl oxidases: from enzyme activity to extracellular matrix cross-links. *Essays Biochem* 2019;**63**:349−64.
21. Yang N, Cao DF, Yin XX, Zhou HH, Mao XY. Lysyl oxidases: emerging biomarkers and therapeutic targets for various diseases. *Biomed Pharmacother* 2020;**131**:110791.
22. Boufraqech M, Zhang L, Nilubol N, Sadowski SM, Kotian S, Quezado M, et al. Lysyl oxidase (LOX) transcriptionally regulates SNAI2 expression and TIMP4 secretion in human cancers. *Clin Cancer Res* 2016;**22**:4491−504.
23. Yehezkely RG, Zaffryar-Eilot S, Kaganovsky A, Malka NF, Aviram R, Livneh I, et al. Intracellular role for the matrix-modifying enzyme lox in regulating transcription factor subcellular localization and activity in muscle regeneration. *Dev Cell* 2020;**53**:406−17.e5.
24. Treissman J, Yuan V, Baltayeva J, Le HT, Castellana B, Robinson WP, et al. Low oxygen enhances trophoblast column growth by potentiating differentiation of the extravillous lineage and promoting LOX activity. *Development* 2020;**147**:dev181263.
25. Wilhelmus MM, Bol JG, van Duinen SG, Drukarch B. Extracellular matrix modulator lysyl oxidase colocalizes with amyloid-beta pathology in Alzheimer's disease and hereditary cerebral hemorrhage with amyloidosis—Dutch type. *Exp Gerontol* 2013;**48**:109−14.
26. Gilad GM, Kagan HM, Gilad VH. Evidence for increased lysyl oxidase, the extracellular matrix-forming enzyme, in Alzheimer's disease brain. *Neurosci Lett* 2005;**376**:210−4.
27. Li PA, He Q, Cao T, Yong G, Szauter KM, Fong KS, et al. Up-regulation and altered distribution of lysyl oxidase in the central nervous system of mutant SOD1 transgenic mouse model of amyotrophic lateral sclerosis. *Brain Res Mol Brain Res* 2004;**120**:115−22.
28. Wong JC, Shapiro L, Thelin JT, Heaton EC, Zaman RU, D'Souza MJ, et al. Nanoparticle encapsulated oxytocin increases resistance to induced seizures and restores social behavior in Scn1a-derived epilepsy. *Neurobiol Dis* 2021;**147**:105147.
29. Yang T, Hu Y, Miao J, Chen J, Liu J, Cheng Y, et al. A BRD4 PROTAC nanodrug for glioma therapy *via* the intervention of tumor cells proliferation, apoptosis and M2 macrophages polarization. *Acta Pharma Sin B* 2022;**12**:2658−71.
30. Khan NU, Ni J, Ju X, Miao T, Chen H, Han L. Escape from abluminal LRP1-mediated clearance for boosted nanoparticle brain delivery and brain metastasis treatment. *Acta Pharm Sin B* 2021;**11**:1341−54.
31. Drysdale ND, Matthews E, Schuetz E, Pan E, McNamara JO. Intravenous kainic acid induces status epilepticus and late onset seizures in mice. *Epilepsy Res* 2021;**178**:106816.
32. Joshi S, Rajasekaran K, Sun H, Williamson J, Kapur J. Enhanced AMPA receptor-mediated neurotransmission on CA1 pyramidal neurons during status epilepticus. *Neurobiol Dis* 2017;**103**:45−53.
33. Ahnstedt H, Mostajeran M, Blixt FW, Warfvinge K, Ansar S, Krause DN, et al. U0126 attenuates cerebral vasoconstriction and improves long-term neurologic outcome after stroke in female rats. *J Cerebr Blood Flow Metabol* 2015;**35**:454−60.
34. Welliver 2nd RC, Hintz KH, Glori M, Welliver RC, Sr. Zileuton reduces respiratory illness and lung inflammation, during respiratory syncytial virus infection, in mice. *J Infect Dis* 2003;**187**:1773−9.
35. Qi J, Kim JW, Zhou Z, Lim CW, Kim B. Ferroptosis affects the progression of nonalcoholic steatohepatitis *via* the modulation of lipid peroxidation-mediated cell death in mice. *Am J Pathol* 2020;**190**:68−81.
36. Barry-Hamilton V, Spangler R, Marshall D, McCauley S, Rodriguez HM, Oyasu M, et al. Allosteric inhibition of lysyl oxidase-like-2 impedes the development of a pathologic microenvironment. *Nat Med* 2010;**16**:1009−17.
37. Li Q, Han X, Lan X, Gao Y, Wan J, Durham F, et al. Inhibition of neuronal ferroptosis protects hemorrhagic brain. *JCI Insight* 2017;**2**:e90777.
38. Friedmann Angeli JP, Schneider M, Proneth B, Tyurina YY, Tyurin VA, Hammond VJ, et al. Inactivation of the ferroptosis regulator Gpx4 triggers acute renal failure in mice. *Nat Cell Biol* 2014;**16**:1180−91.
39. Racine RJ. Modification of seizure activity by electrical stimulation. II. Motor seizure. *Electroencephalogr Clin Neurophysiol* 1972;**32**:281−94.
40. Scalisi J, Balau B, Deneyer L, Bouchat J, Gilloteaux J, Nicaise C. Blood−brain barrier permeability towards small and large tracers in a mouse model of osmotic demyelination syndrome. *Neurosci Lett* 2021;**746**:135665.
41. Zhao J, Ye Z, Yang J, Zhang Q, Shan W, Wang X, et al. Nanocage encapsulation improves antiepileptic efficiency of phenytoin. *Biomaterials* 2020;**240**:119849.
42. Zhang X, Liu W, Yuan J, Zhu H, Yang Y, Wen Z, et al. T lymphocytes infiltration promotes blood−brain barrier injury after experimental intracerebral hemorrhage. *Brain Res* 2017;**1670**:96−105.
43. Chu C, Jablonska A, Gao Y, Lan X, Lesniak WG, Liang Y, et al. Hyperosmolar blood−brain barrier opening using intra-arterial injection of hyperosmotic mannitol in mice under real-time MRI guidance. *Nat Protoc* 2022;**17**:76−94.
44. Okuyama M, Jiang W, Javidan A, Chen JZ, Howatt DA, Yang L, et al. Lysyl oxidase inhibition ablates sexual dimorphism of abdominal aortic aneurysm formation in mice. *Circulation* 2020;**142**:1993−5.
45. Martínez-Revelles S, García-Redondo AB, Avendaño MS, Varona S, Palao T, Orriols M, et al. Lysyl oxidase induces vascular oxidative stress and contributes to arterial stiffness and abnormal elastin structure in hypertension: role of p38MAPK. *Antioxid Redox Signal* 2017;**27**:379−97.
46. Liu Y, Wang W, Li Y, Xiao Y, Cheng J, Jia J. The 5-lipoxygenase inhibitor zileuton confers neuroprotection against glutamate oxidative damage by inhibiting ferroptosis. *Biol Pharm Bull* 2015;**38**:1234−9.
47. Jiang L, Kon N, Li T, Wang SJ, Su T, Hibshoosh H, et al. Ferroptosis as a p53-mediated activity during tumour suppression. *Nature* 2015;**520**:57−62.
48. Dingledine R, Varvel NH, Dudek FE. When and how do seizures kill neurons, and is cell death relevant to epileptogenesis?. *Adv Exp Med Biol* 2014;**813**:109−22.
49. Fitzharris TP, Markwald RR, Dunn BE. Effects of beta-aminopropionitrile fumurate (BAPN) on early heart development. *J Mol Cell Cardiol* 1980;**12**:553−77.
50. Martin JE, Sosa-Melgarejo JA, Swash M, Mather K, Leigh PN, Berry CL. Purkinje cell toxicity of beta-aminopropionitrile in the rat. *Virchows Arch A Pathol Anat Histopathol* 1991;**419**:403−8.
51. Xue CC, Li MH, Zhao Y, Zhou J, Hu Y, Cai KY, et al. Tumor microenvironment-activatable Fe-doxorubicin preloaded amorphous $CaCO_3$ nanoformulation triggers ferroptosis in target tumor cells. *Sci Adv* 2020;**6**:eaax1346.
52. Pitkänen A, Nissinen J, Nairismägi J, Lukasiuk K, Gröhn OH, Miettinen R, et al. Progression of neuronal damage after status epilepticus and during spontaneous seizures in a rat model of temporal lobe epilepsy. *Prog Brain Res* 2002;**135**:67−83.
53. Payne SL, Fogelgren B, Hess AR, Seftor EA, Wiley EL, Fong SF, et al. Lysyl oxidase regulates breast cancer cell migration and adhesion through a hydrogen peroxide-mediated mechanism. *Cancer Res* 2005;**65**:11429−36.
54. Rachman-Tzemah C, Zaffryar-Eilot S, Grossman M, Ribero D, Timaner M, Mäki JM, et al. Blocking surgically induced lysyl oxidase activity reduces the risk of lung metastases. *Cell Rep* 2017;**19**:774−84.
55. Tang H, Leung L, Saturno G, Viros A, Smith D, Di Leva G, et al. Lysyl oxidase drives tumour progression by trapping EGF receptors at the cell surface. *Nat Commun* 2017;**8**:14909.
56. Gilad GM, Gilad VH. Beta-aminopropionitrile treatment can accelerate recovery of mice after spinal cord injury. *Eur J Pharmacol* 2001;**430**:69−72.
57. Li J, Gu X, Ma Y, Calicchio ML, Kong D, Teng YD, et al. Nna1 mediates purkinje cell dendritic development *via* lysyl oxidase propeptide and NF-κB signaling. *Neuron* 2010;**68**:45−60.
58. Satoh T, Nakatsuka D, Watanabe Y, Nagata I, Kikuchi H, Namura S. Neuroprotection by MAPK/ERK kinase inhibition with U0126 against oxidative stress in a mouse neuronal cell line and rat primary cultured cortical neurons. *Neurosci Lett* 2000;**288**:163−6.

59. Werz O, Bürkert E, Fischer L, Szellas D, Dishart D, Samuelsson B, et al. Extracellular signal-regulated kinases phosphorylate 5-lipoxygenase and stimulate 5-lipoxygenase product formation in leukocytes. *FASEB J* 2002;**16**:1441−3.
60. Sun QY, Zhou HH, Mao XY. Emerging roles of 5-lipoxygenase phosphorylation in inflammation and cell death. *Oxid Med Cell Longev* 2019;**2019**:2749173.
61. Steinhilber D, Hofmann B. Recent advances in the search for novel 5-lipoxygenase inhibitors. *Basic Clin Pharmacol Toxicol* 2014;**114**:70−7.
62. Giannopoulos PF, Praticò D. Overexpression of 5-lipoxygenase worsens the phenotype of a mouse model of tauopathy. *Mol Neurobiol* 2018;**55**:5926−36.
63. Gener P, Montero S, Xandri-Monje H, Díaz-Riascos ZV, Rafael D, Andrade F, et al. Zileuton™ loaded in polymer micelles effectively reduce breast cancer circulating tumor cells and intratumoral cancer stem cells. *Nanomedicine* 2020;**24**:102106.
64. Chu J, Li JG, Praticò D. Zileuton improves memory deficits, amyloid and tau pathology in a mouse model of Alzheimer's disease with plaques and tangles. *PLoS One* 2013;**8**:e70991.
65. Yang WS, Kim KJ, Gaschler MM, Patel M, Shchepinov MS, Stockwell BR. Peroxidation of polyunsaturated fatty acids by lipoxygenases drives ferroptosis. *Proc Natl Acad Sci U S A* 2016;**113**:E4966−75.
66. Karuppagounder SS, Alin L, Chen Y, Brand D, Bourassa MW, Dietrich K, et al. *N*-Acetylcysteine targets 5 lipoxygenase-derived, toxic lipids and can synergize with prostaglandin E_2 to inhibit ferroptosis and improve outcomes following hemorrhagic stroke in mice. *Ann Neurol* 2018;**84**:854−72.
67. Kasina V, Mownn RJ, Bahal R, Sartor GC. Nanoparticle delivery systems for substance use disorder. *Neuropsychopharmacology* 2022;**47**:1431−9.
68. Qi C, Lin J, Fu LH, Huang P. Calcium-based biomaterials for diagnosis, treatment, and theranostics. *Chem Soc Rev* 2018;**47**:357−403.
69. Haruta S, Hanafusa T, Fukase H, Miyajima H, Oki T. An effective absorption behavior of insulin for diabetic treatment following intranasal delivery using porous spherical calcium carbonate in monkeys and healthy human volunteers. *Diabetes Technol Ther* 2003;**5**:1−9.